RSC
Chemical Biology

ROYAL SOCIETY
OF **CHEMISTRY**

PAPER
Javier Montenegro *et al.*
Short oligoalanine helical peptides for supramolecular
nanopore assembly and protein cytosolic delivery

Check for updates

Short oligoalanine helical peptides for supramolecular nanopore assembly and protein cytosolic delivery†

Marta Pazo, [ID] [a] Giulia Salluce, [ID] [a] Irene Lostalé-Seijo, [ID] [a] Marisa Juanes, [ID] [a] Francisco Gonzalez, [ID] [bc] Rebeca Garcia-Fandiño [ID] [a] and Javier Montenegro [ID] *[a]

In this work we report a rational design strategy for the identification of new peptide prototypes for the non-disruptive supramolecular permeation of membranes and the transport of different macromolecular giant cargos. The approach targets a maximal enhancement of helicity in the presence of membranes with sequences bearing the minimal number of cationic and hydrophobic moieties. The here reported folding enhancement in membranes allowed the selective non-lytic translocation of different macro-molecular cargos including giant proteins. The transport of different high molecular weight polymers and functional proteins was demonstrated in vesicles and in cells with excellent efficiency and optimal viability. As a proof of concept, functional monoclonal antibodies were transported for the first time into different cell lines and cornea tissues by exploiting the helical control of a short peptide sequence. This work introduces a rational design strategy that can be employed to minimize the number of charges and hydrophobic residues of short peptide carriers to achieve non-destructive transient membrane permeation and transport of different macromolecules.

Introduction

The selective non-destructive and transient disruption of membranes constitutes one of the most important challenges for chemistry and macromolecular transport.[1–4] Cationic natural or synthetic amphiphiles have been widely employed for membrane perturbation due to the presence of anionic lipids or the abundant anionic glycosaminoglycans at the plasma membrane, which are generally involved in the initial interactions between biological membranes and cell penetrating peptides. Therefore, different cationic lipids, biopolymers and synthetic analogues have been employed for the membrane translocation of hydrophilic macromolecules.[1–4] However, strongly cationic molecules and surfactants suffer from non-specific binding to membranes and detergent behavior.[1,5,6] Over the last years,

different strategies employing cationic synthetic materials[3,7,8] have been developed to transport bioactive macromolecules,[9] which include peptides,[10–21] chimeric proteins,[22] polymers,[23–25] dynamic covalent bonds,[23–26] supramolecular caging,[27] transient charge masking,[28] lipid particles,[29,30] polymersomes,[31,32] and highly charged nanoparticles.[33–35] Importantly, the presence of anionic lipids, especially in the endosomal compartments, has been proved critical for the correct function of several natural[36,37] and artificial cationic macromolecular carriers.[12,38] In general, cationic and amphiphilic membrane targeted molecules mainly operate by unspecific disruption of membranes and/or by the direct endosomal annihilation due to osmotic pressure unbalance.[5,39] Nevertheless, most of the recently developed synthetic transporters incorporate a high number of cationic residues and/or show strong amphiphilic character, which can easily destroy membranes and cause toxicity.[6,40] Despite a high number of charges could interfere with anionic biomolecules and cause toxicity, certain reported peptides reduce these limitations by controlling their membranolytic activity, such as RALA,[41] which requires endosomal pH acidification. Despite these clear precedents, little attention has been focused on the development of rational strategies for the design of membrane targeted molecules with selective and transient non-lytic membrane disruption and with a minimum number of cationic and hydrophobic residues.[6] Herein, we report a rational strategy for non-disruptive membrane permeation and macromolecular transport, which is based on the

[a] Centro Singular de Investigación en Química Bioloxica e Materiais Moleculares (CIQUS), Departamento de Química Orgánica, Universidade de Santiago de Compostela, 15782, Santiago de Compostela, Spain.
E-mail: javier.montenegro@usc.es
[b] Centro Singular de Investigación en Medicina Molecular y Enfermedades Crónicas (CIMUS), Universidade de Santiago de Compostela, 15782, Santiago de Compostela, Spain
[c] Instituto de Investigación Sanitaria de Santiago de Compostela (IDIS) and Service of Ophthalmology, Complejo Hospitalario Universitario de Santiago, 15706 Santiago de Compostela, Spain

maximization of the helicity of a short, simple peptide as it transits from the aqueous to the membrane environment. Experiments in vesicles and dynamic simulations confirmed the targeted peptide helical enhancement and the non-lytic membrane permeation, which triggered the non-covalent transport of different cargos through the membranes of vesicles and cells. This strategy allowed the discovery of a peptide sequence, with only three arginine residues, which transported, with high efficiency and low toxicity, functional proteins and monoclonal antibodies across membranes of cells and tissues.

Results

Design and initial screening

Seminal work from Baldwin and co-workers highlighted the importance of alanine residues to promote helical folding in short peptides in the absence of side chain stabilizing interactions.[43,44] In addition, inspiring cationic penetrating oligoalanine scaffolds, originally reported by Steven Dowdy,[45] had been shown to efficiently internalize inside cells.[46] In these scaffolds, four helical turns are required to quantify helicity by a measurable Cotton effect in circular dichroism (CD).[45,46] Therefore, sequences of 16 amino acids were selected to study and optimize peptide helical folding in different environments.[42]

We started from short peptide scaffolds of alanine, the amino acid with the strongest alpha helical stabilizing character, to adjust the minimal number of substitutions by cationic (Arg) and hydrophobic (Leu) aminoacids that would endow the peptide with penetrating properties. Minimization of cationic residues was targeted in order to reduce the potential complexation with anionic biopolymers[47] and three leucines were previously found to maximize peptide uptake.[46] Thus, in this work, three oligo-alanine peptides[46] with different and representative helical behavior[43] (**MP1**, **MP2** and **P3**) were designed and synthesized together with the octaarginine **Arg$_8$** and the pore-forming **GALA**, as peptide controls with higher cationic and hydrophobic character respectively (Fig. 1a). The CD spectra indicated that the minimal peptide **MP1**, with three aligned arginines and a radial distribution of three leucines close to the N-terminus (Fig. 1a–c), showed low helicity in aqueous buffer that was increased (to 20%) in the presence of zwitterionic neutral liposomes (POPC: 1-palmitoyl-2-oleoylphosphatidylcholine) (Fig. 1d and Fig. S1, ESI†). In contrast, peptide **MP2** with three aligned arginines and three aligned leucines, on the same side of the putative alpha helix, showed stronger helical behaviour in buffer ($\sim$20%) that was reduced ($\sim$10%) in neutral lipid membranes (Fig. 1d and Fig. S1, ESI†). Peptide **P3**, analogous to **MP1** but with one extra helical turn (Fig. 1a), showed higher helicity in buffer ($\sim$35%) that was also enhanced in liposomes ($\sim$50%), close to the maximum
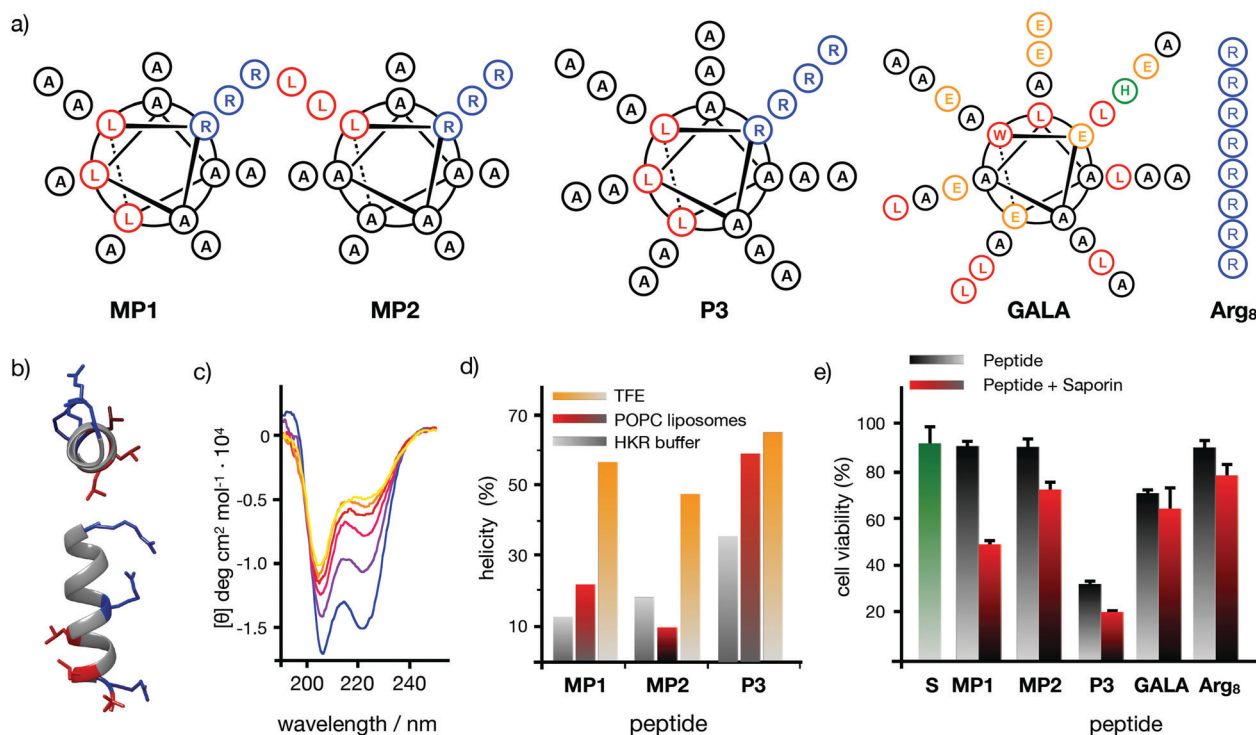
Fig. 1 Peptide structures, helical content quantification by CD and initial screening. (a) Peptides' structures. Sequences: **MP1** (Ac-LRALAALARAAAAAR-NH$_2$); **MP2** (Ac-LRAAAAALRAAAAALR-NH$_2$); **P3** (Ac-LRALAALARAAAAAARAAAAAAR-NH$_2$); **GALA** (Ac-WEAALAEALAEALAEHLAEALAEALEALAA-NH$_2$); **Arg$_8$** (Ac-RRRRRRRR-NH$_2$), (b) 3D prediction of **MP1** using PEP-FOLD 3.5.[42] Arginines in blue, leucines in red. (c) Circular dichroism spectra of **MP1** (100 μM) at different temperatures (10, 20, 30, 40, 50, 60 °C) in HKR buffer. (d) % helicity of **MP1**, **MP2**, and **P3** in HKR, liposomes (POPC) or TFE at 40 °C (see ESI†). (e) Cell viability in HeLa cells without (grey) or with (red) 10 μg mL^{-1} of saporin and 30 μM of the indicated peptides for 1 h and further incubation for 6 h before measuring viability by MTT assay. In green the control with saporin alone. Error bars represent standard deviation (SD) of 3 replicates.
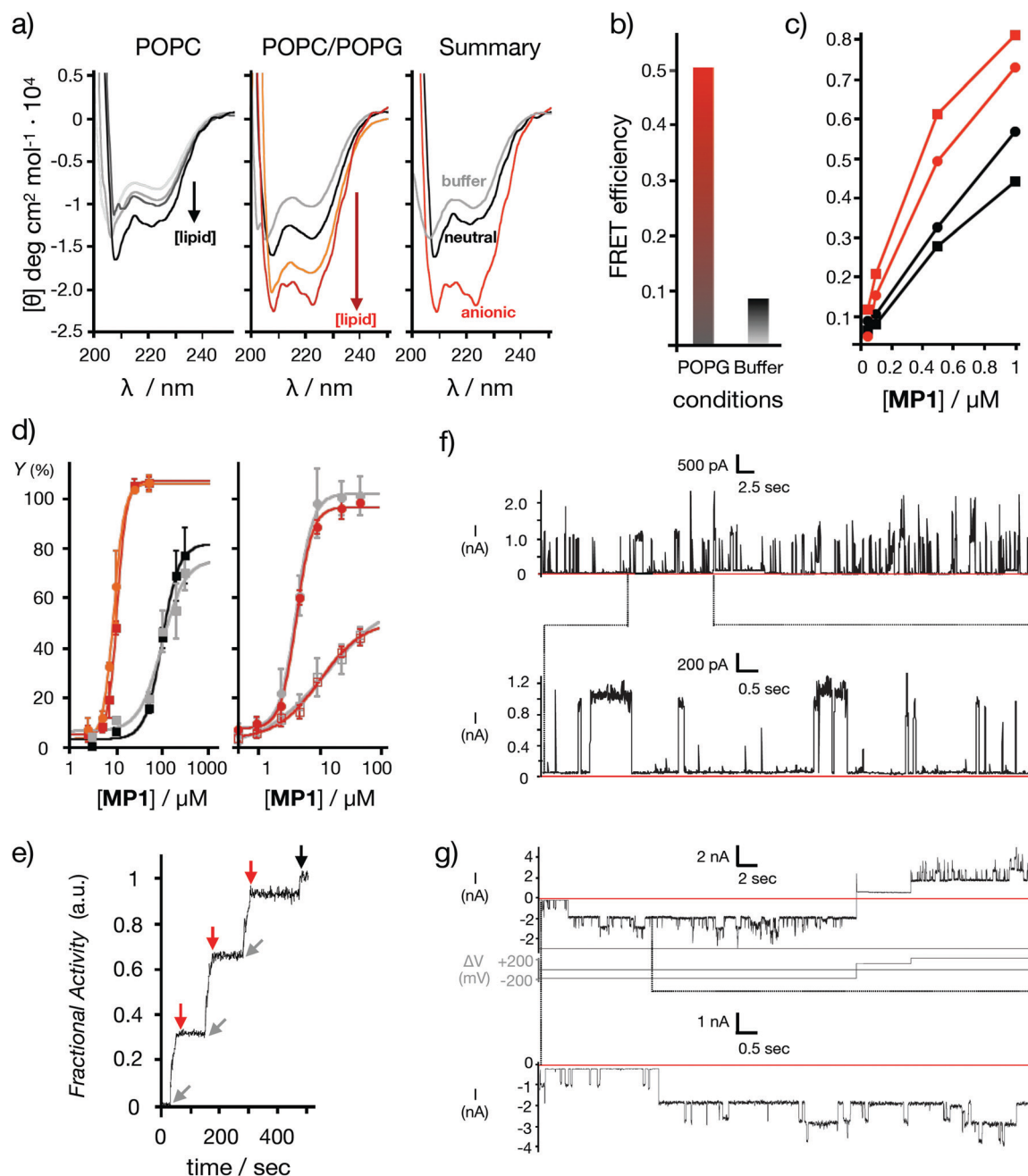
Fig. 2 Model membranes. (a) Peptide helicity at pH 7.5 (20 °C) in the presence of neutral vesicles (left) and anionic vesicles (middle) with different lipid/peptide ratios (L/P: 1.25, 5, 12, 50). On the right a summary of the CD spectra with buffer (grey), neutral (black) and anionic (red) vesicles at L/P 50 is shown. (b) FRET efficiency between the labelled peptides: **CF-MP1** (donor) and **TM-MP1** (acceptor), in anionic vesicles (red) and aqueous buffer (grey). [Peptides] = 5 μM each, [vesicles] = 125 μM. (c) FRET efficiency between the NBD labelled phospholipid (donor) and the labelled peptide **TM-MP1** (acceptor) in neutral (black) or anionic (red) vesicles. Circles are for head- and squares for the tail-labelled NBD-lipid. [Vesicles] = 125 μM. (d) Left: Dose response curves for LUVs⊂ANTS/DPX release experiments at different **MP1** concentrations. Anionic vesicles are in red (pH 7.5) and in orange (pH 5.5) (EC$_{50}$ = 10.7 and 9.0 μM respectively). Neutral vesicles are in black (pH 7.5) and in grey (pH 5.5) (EC$_{50}$ = 98.2 and 97.2 μM respectively). Right: Dose response curves for dextran release in anionic vesicles LUVs⊂Dextran at different **MP1** concentrations. The 10 kDa FITC-Dex (filled circles) and 40 kDa TM-Dex (empty squares) are shown in red (pH 7.5) and in grey (pH 5.5) respectively. Fractional activity Y against peptide concentration (n = 3). (e) BLM electrical current recordings in DPhPC membrane at 25 μM of peptide in each well (potential in first recording +200 mV; in second recording, +200 mV or −200 mV as indicated). Conditions: 0.5 M KCl, 10 mM MOPS, pH 7.4. The current signals were aquired at 1 kHz and sampled at 5 kHz, resulting data were filtered using low pass Bessel (8-pole). Kinetic fluorescent trace of LUVs⊂ANTS/DPX showing cycles of pore gating at pH 7.5 after sequential additions of **MP1** (gray arrows, 10 μM at t = 25, 150, and 275 s) and POPG (red arrows, 50 μM at t = 50, 175, and 300 s). At t = 475 s (black arrow) Triton X-100 was added for complete vesicle lysis (see ESI†).

helicity that can be detected with the helix-stabilizing solvent TFE.[48] With these three representative examples of our previously

reported library of penetrating oligoalanines,[46] a preliminary screening of the uptake and cytosolic release of a cell-impermeable

© 2021 The Author(s). Published by the Royal Society of Chemistry

RSC Chem. Biol., 2021, 2, 503–512 | 505

toxin was carried out by the MTT assay (Fig. 1e). Incubation of all peptides with cells, in the absence or in the presence of saporin, indicated optimal transport of the toxin for **MP1**, lower efficiency for **MP2** and strong toxicity of the longer most helical oligoalanine **P3** (Fig. 1e). The corresponding control experiments with **GALA**[49] and **Arg$_8$**[5] showed lower levels of saporin uptake and release (Fig. 1e).

## Selective membrane disruption by MP1

This interesting toxin transport profile and the previously confirmed maximal uptake of **MP1** in cells[46] prompted a detailed characterization of the interactions of this peptide in different lipid bilayer membranes (Fig. 2). To study the impact of anionic lipids,[37,50] the CD of **MP1** was measured in anionic vesicles (POPC/POPG 3 : 1, POPG: 1-palmitoyl-2-oleoyl-*sn*-glycero*-3-phosphoglycerol, Fig. 2a). A remarkable four-fold helicity enhancement was observed in the transition of **MP1** from aqueous to anionic lipid environments (Fig. 2a).[37] Fluorescence resonance energy transfer (FRET) between the peptide labelled with a carboxyfluorescein probe (**CF-MP1**, donor) and the peptide labelled with TAMRA (**TM-MP1**, acceptor), indicated a much higher self-assembly of **MP1** in the presence of anionic membranes compared to that of the aqueous buffer (Fig. 2b). Self-assembly of **MP1** in the absence of membranes is supported by the quenching and red shift of the emission of a carboxyfluorescein labelled **MP1** at increasing concentrations (Fig. S2, ESI†). FRET experiments with the donor partner (nitrobenzoxadiazole, NBD) installed in a phospholipid counterpart confirmed a higher FRET, and thus membrane affinity, between the TAMRA-labelled peptide (**TM-MP1**) with anionic vesicles in comparison to neutral vesicles (Fig. 2c).

Analogous FRET experiments but with the NBD donor installed in the alkyl chain of the lipid counterpart indicated a preferential orientation of the **MP1** peptide with the hydrophobic leucine N-terminus deeply inserted into the non-polar region of the bilayer (Fig. 2c). Release experiments were then performed in large unilamellar vesicles with an encapsulated fluorescent probe and a quencher (LUVs⊂ANTS/DPX, ∼120 nm).[38] Dose–response experiments with **MP1** showed a strong selectivity for negatively charged membranes, as indicated by a ten times lower EC$_{50}$ for probe release in anionic vesicles (POPC/POPG 3 : 1) compared to neutral liposomes (POPC) (Fig. 2d (left) and Fig. S3a, ESI†). High molecular weight dextran (*i.e.* 10–40 kDa) *in vitro* release experiments in vesicles revealed marginal dextran release from neutral vesicles but efficient and size-selective leakage of dextran polymers for anionic vesicles (Fig. 2d (right) and Fig. S3b, ESI†).[2] Importantly, dynamic light scattering (DLS) measurements of the vesicles in the presence of **MP1** confirmed the homogenous size and structural integrity of the vesicles even at very high peptide concentrations (*i.e.* 800 μM, Fig. S3c, ESI†). These results confirmed a non-destructive membrane disruption mechanism enhanced by the specific folding and the supramolecular assembly of **MP1**.

Computational modelling

Computational simulations were performed to study **MP1** in the highly dynamic environment of the early endosomal membrane (see ESI†). As experimentally confirmed by CD, the atomistic Molecular Dynamics (AT-MD) simulations of **MP1**

revealed peptide unfolding in aqueous solution and stable helical arrangement in TFE (Fig. 3a). AT-MD simulations are restricted to short timescales, which hinder the observation of multiple peptide folding, aggregation and membrane insertion events.[51] Alternatively, coarse-grained (CG-MD) simulations largely increase the computational power and timescales, allowing the simulation of complex dynamic systems. Accordingly, CG-MD simulations using the MARTINI force-field[52] were performed starting from different folded units of **MP1** in an early endosome anionic model membrane in the presence of an external electric field simulating the endosomal membrane potential (Fig. 3b–d and Fig. S4, ESI†).[53] 31 units of **MP1** in the presence of 1309 lipids, L/P ∼ 42, were used to achieve a L/P ratio corresponding to the lowest active peptide concentration in the vesicle leakage experiments (∼3 μM, Fig. 2d). These experiments confirmed the initial interaction of **MP1** with membranes by anchoring and orienting the Leu enriched hydrophobic N-terminus towards the hydrophobic core of the lipid bilayer, and the arginine cationic residues exposed to the solvent environment (Video S1, ESI†), as experimentally supported by FRET (Fig. 2c). Interestingly, beyond the strong interactions with the membrane, adaptive peptide **MP1**
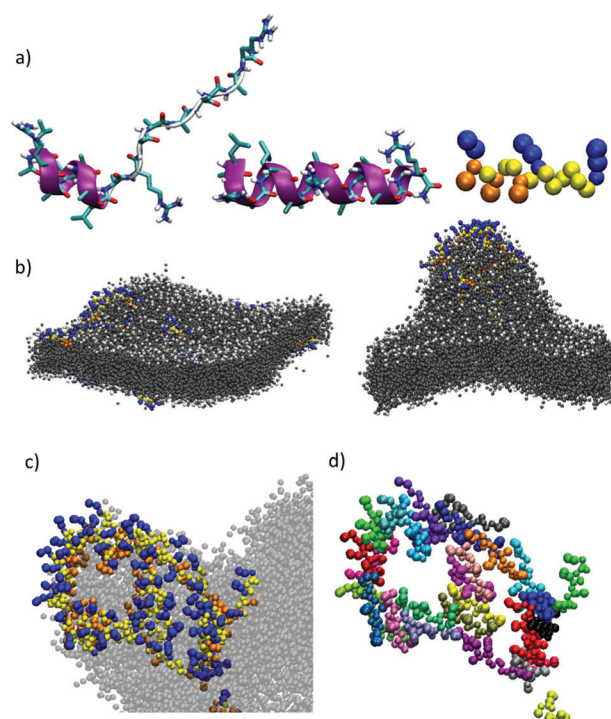

Fig. 3 (a) Snapshot (*t* = 40 ns) from AT-MD simulations of peptide **MP1** in water (left), TFE (middle) and mapping to CG resolution (right). (b) Snapshots from CG-MD simulations [*t* = 10 ns, (left) and *t* = 300 ns (right) respectively] showing the interaction of peptides and an asymmetric bilayer composed by DPPC : DPPE (9 : 1) and DPPC : DPPE : DPPS (3 : 5 : 2), subjected to an external electric field of 30 mV applied across the membrane. A detail of the disposition of the peptides (c and d) is shown. CG residues in (b and c) are represented in yellow (Ala), orange (Leu) and blue (Arg). A different color is used for each peptide in (d) to highlight the independent units of **MP1**. (DPPC: dipalmitoyl phosphatidylcholine, DPPE: dipalmitoyl phosphatidylethanolamine, DPPS: dipalmitoyl phosphatidylserine).

showed a self-assembly pattern with the Ala residues interacting between peptide monomers and mimicking prefibrillar peptide assemblies in the lipid bilayer (Fig. 3b–d). The self-assembly of the peptides, in a model membrane with external applied electric field, showed the inducement of local membrane curvature and self-assembly of **MP1** at the apical regions of the membrane invaginations (Fig. 3b–d). As the simulation evolved with time, a transitory membrane disruption was observed (Fig. 3c, d and Fig. S4, ESI†).

To investigate the potential formation of membrane pores by **MP1**, gating experiments were carried out by sequential addition to vesicles of **MP1** followed by an anionic binder competitor (POPG). Pore gating (opening/closing) was confirmed by three cycles of activation and inhibition of the transport in a single transport kinetics experiment (Fig. 2f). Finally, to unambiguously confirm the potential assembly of supramolecular nanopores from **MP1**, ion channel conductance recordings were performed in planar bilayer membranes (black lipid membranes, BLM).[54] The typical BLM current

recordings reported for oligocationic penetrating peptides (*i.e.* nonarginine) have shown random spikes of current, whose noise fluctuations increased with time.[55] In contrast, recordings of **MP1** showed individual stochastic gating events of high current, which were indicative of the formation of individual giant channels assembled from **MP1** (see ESI† and Fig. 2e). Not surprisingly, as previously shown for other membrane ion channels,[56] the formation of **MP1** channels was dependent on the applied voltage. However, the remarkably high and identical steady state current intensity ($\sim$1100 pA, 200 mV) of the series of stochastic events, observed along different BLM recordings, demonstrated the assembly of a hitherto not described giant supramolecular membrane pore assembled from a peptide sequence shorter than a membrane leaflet. Intriguingly, the integrity of the planar bilayer was maintained even at long times with **MP1** (Fig. 2e) and current recordings eventually showed long-lasting opened states (at 1900 pA) with additional individual stochastic gating events of identical current intensity (1100 pA) on top of the opened state (Fig. 2e).
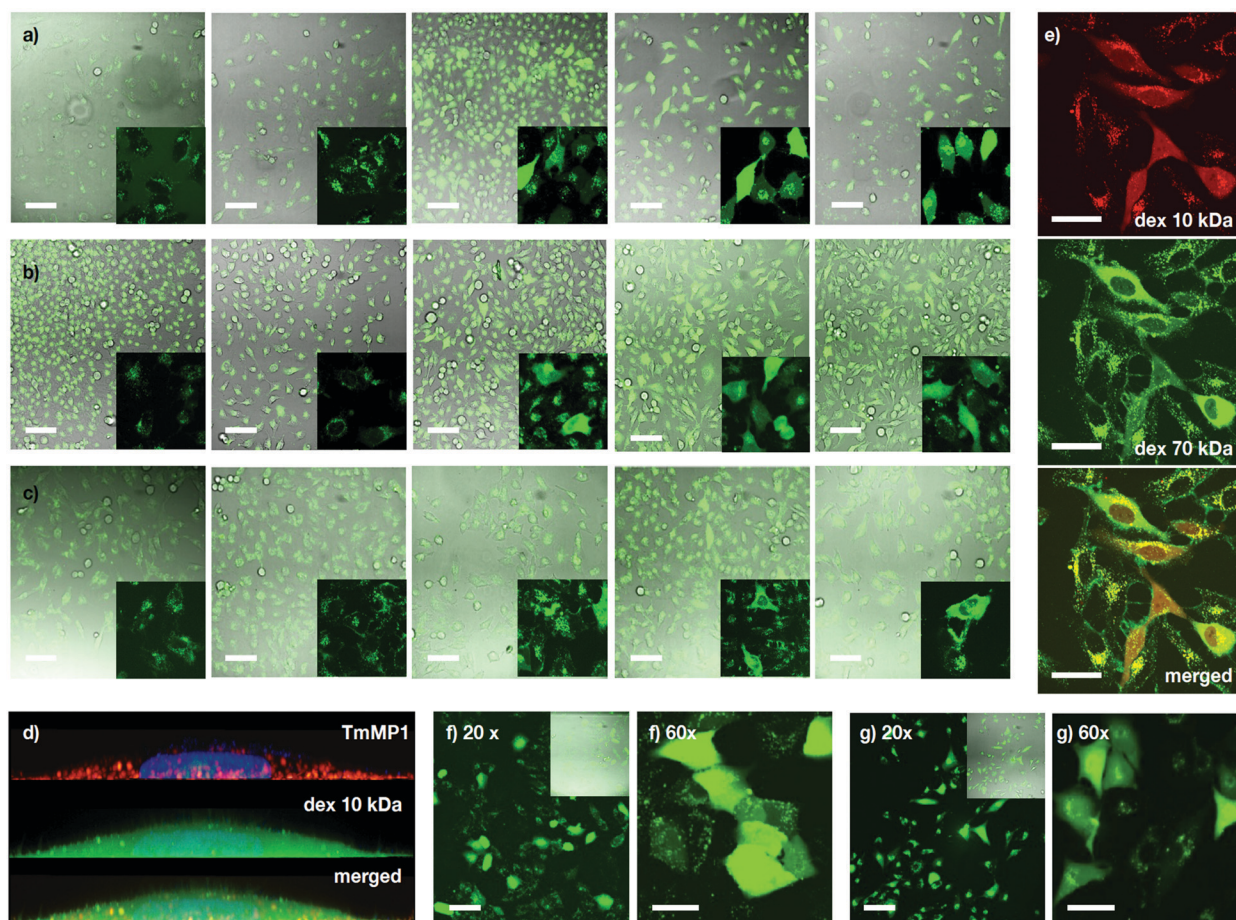
Fig. 4 Dextran (Dex) transport. (a–c) HeLa cells incubated with **MP1** (0, 10, 20, 30, 50 µM) and fluorescently labelled dextran: 10 kDa Alexa488-Dex (a), 40 kDa FITC-Dex (b) and 70 kDa FITC-Dex (c). In the absence of **MP1**, punctate fluorescence signal was observed, which is indicative of endosomes or lysosomes. Peptide-triggered cytosolic release of the dextran affords a homogeneous staining of the cell. Percentage of cells with intracellular release at 30 µM was 42, 30 and 10% for (a, b and c). (d) 3D view of a HeLa cell with 5 µM **TM-MP1** (orange) and 10 kDa Alexa488-Dex (green), showing dextran (cytosol) and peptide (endosomes). Nucleus stained with Hoechst. (e) HeLa cells co-incubated with 10 kDa TM-Dex (red), 70 kDa FITC-Dex (green) and **MP1** (30 µM). (f) Vero cells with 10 kDa Alexa488-Dex and 20 µM **MP1** (30% release). (g) A549 cells with 10 kDa Alexa488-Dex and 50 µM of **MP1** (30% release). Scale bars are 100 µm for (a–c and f) (20×), (g) (20×) and 50 µm for (e and f) (60×) and (g) (60×).

© 2021 The Author(s). Published by the Royal Society of Chemistry

RSC Chem. Biol., 2021, **2**, 503–512 | **507**

Dextran transport in cells

Following the preliminary transport results and the excellent properties of **MP1** in model membranes, transport experiments in cells were investigated first with dextran polymers, which are markers of endocytic routes, and are unable to escape from the endosome on their own.[9,57] Kinetic experiments in HeLa cells showed mainly punctate fluorescence at short incubation times (*i.e.* 1 hour) and LysoTracker staining indicated that **TM-MP1** and dextran remained trapped together in the endosomes (punctated pattern, Fig. 4d and Fig. S5, ESI†). Despite the peptide did not leave the endosomes, at longer incubation times (3 hours) stronger diffuse cytosolic dextran fluorescence was detected inside the cells, which suggested an initial endocytic uptake followed by dextran release (Fig. S5, ESI†).

Experiments with dextran polymers of different molecular weights (10, 40 and 70 kDa) showed excellent, yet size-selective cytosolic transport of the different dextrans for **MP1** at 20 and 30 μM concentration (Fig. 4a–c).[58] Mixed solutions of different dextrans again confirmed simultaneous and size selective polymer transport (10 > 70 kDa, Fig. 4e). Importantly, polymer transport was insensitive to the presence of serum proteins, as the same level of dextran uptake and release, about 45%, was confirmed in the presence of 10% FBS (Fig. S6a, ESI†). In addition, we had previously determined that **TM-MP1** half-life in 100% FBS was ∼2.2 h.[46] Vero (monkey kidney) and the difficult-to-transfect A549 (human lung cancer) cells further confirmed the excellent scope of **MP1** (Fig. 4f and g). Studies in the presence of endocytic inhibitors showed only partial inhibition of the uptake and intracellular release, which requires the uptake of both peptide and dextran, by dynasore and EIPA, which block dynamin-dependent endocytosis and macropinocytosis respectively (Fig. S6b, ESI†). Therefore, as these routes are well known to be responsible for the dextran polymer uptake,[57] these results suggested a mixed uptake for **MP1** and a general mechanism for the transport of the polymers, which was mainly dependent on the uptake of the dextran cargo.
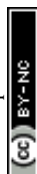
Functional protein transport in cells

The excellent profile for the membrane transport of **MP1** with model hydrophilic polymers prompted the study of functional protein cargos (Fig. 5 and Fig. S7, ESI†). Dose response transport experiments with **MP1** (0–50 μM) in HeLa cells in the presence or absence of saporin (10 μg mL⁻¹) showed a respectable 70% toxicity enhancement for **MP1** and perfect cell viability for the peptide alone in the absence of the toxin (Fig. 5a). Control experiments showed minor transport for the **GALA** peptide and no activity for **Arg₈** after 6 h incubation (Fig. S7a, ESI†). Further control experiments, at longer recovery times (24 hours), showed the enhanced saporin cytosolic transport in HeLa (Fig. S7b, ESI†) and A549 cells (Fig. S7c, ESI†).

The Cre recombinase enzyme catalyses *loxP* sites recombination followed by gene expression switch from a red (dsRED) to a green (EGFP) fluorescent protein in a reporter cell line (Fig. 5b, c and Fig. S8, ESI†).[59] The corresponding microscopy and flow cytometry quantification of the Cre transport in HeLa cells confirmed an excellent level of recombination at low concentrations of **MP1**, optimal at 10 μM and superior to the controls with **Arg₈** and **GALA** (Fig. 5b and c). Finally, supramolecular
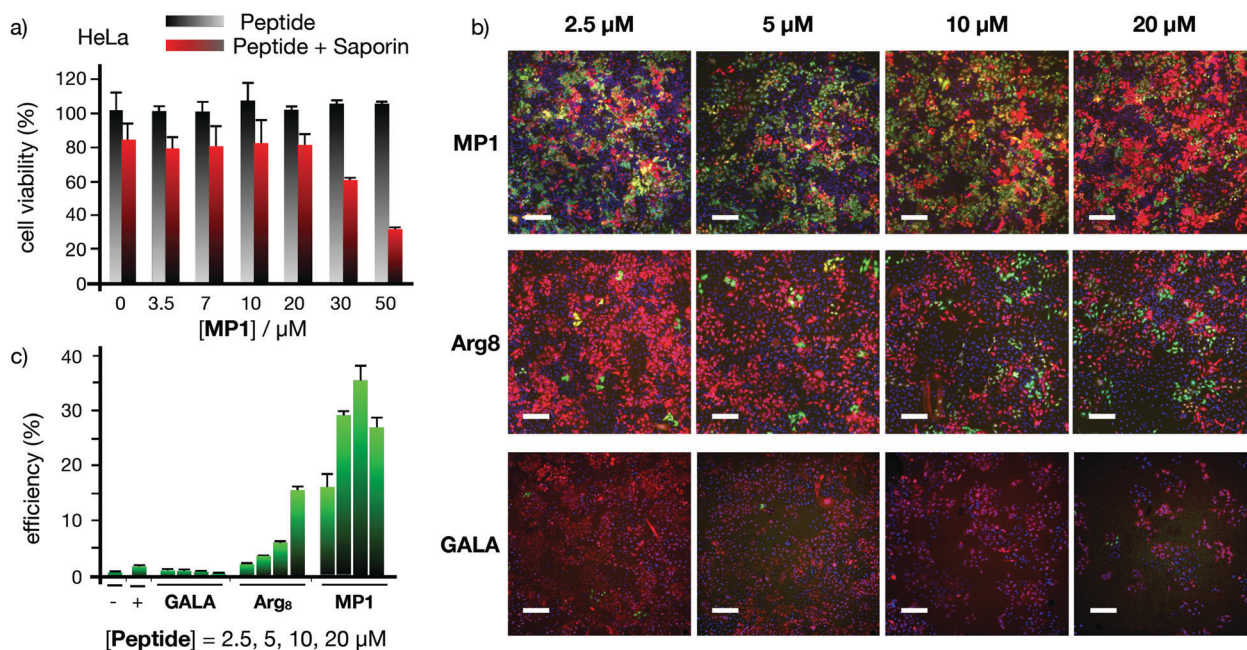
Fig. 5 Functional protein membrane transport. (a) HeLa cells incubated with 0 (grey bars) or 10 μg mL⁻¹ (red bars) saporin in the presence of increasing concentrations of **MP1** for 1 h, medium was then replaced and cells further incubated for 6 h before measuring viability by MTT assay. (b) Cre reporter-HeLa cells 3 days after incubation with the indicated peptides (**MP1**, **Arg₈**, or **GALA**) and Cre recombinase. Cre recombination turned the dsRED (red) to EGFP (green) expression. Nuclei stained with Hoechst (blue). Scale bars are 200 μm. (c) Flow cytometry quantification of the fraction of EGFP expressing Cre reporter-HeLa cells. Error bars represent SD of three replicates.

508 | *RSC Chem. Biol.*, 2021, **2**, 503–512

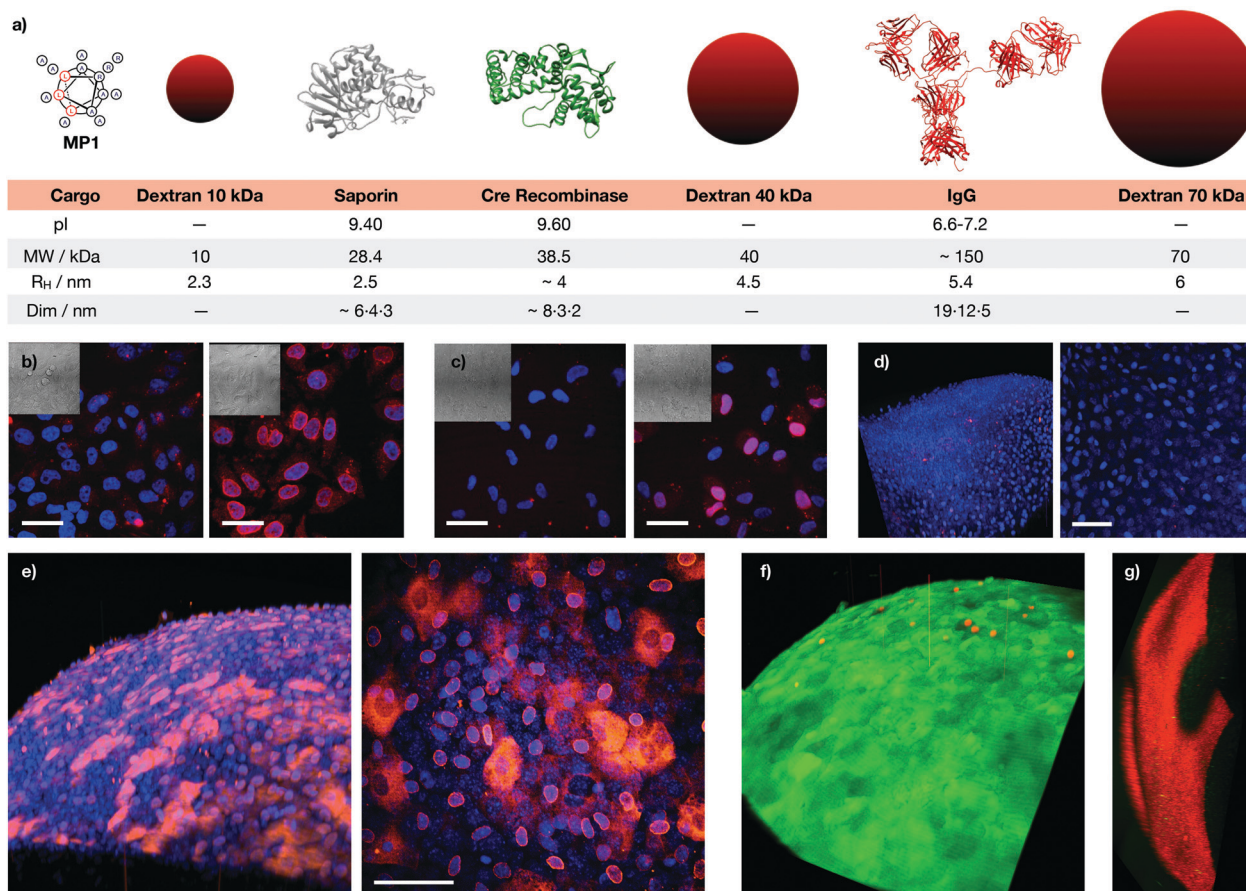© 2021 The Author(s). Published by the Royal Society of Chemistry

transport experiments with green fluorescent protein (GFP) equipped with a nuclear localization signal (NLS) also confirmed the transport of this functional cargo by cell's nuclei staining due to GST-NLS-GFP accumulation (Fig. S9a, ESI†). Importantly, independent MTT toxicity assays confirmed that the IC_{50} toxicity values obtained for **MP1** were between four and ten-fold higher than the optimal **MP1** release concentration (30 μM and 10 μM for dextran and Cre recombinase respectively, Fig. S10–S12, ESI†). This remarkable ratio in the active/toxic concentration of **MP1** confirmed the integrity of the plasma membrane and the non-lytic efficient transport of large macromolecules in live cells.

Transport of antibodies

These excellent results encouraged us to test the potential of the helical responsive **MP1** for the transport of antibodies,[5–7,40,60,61] which was evaluated with mouse monoclonal Mab414 against the nuclear pore complex proteins (Fig. 6 and Fig. S14, see ESI†). Transport of Mab414 and its functional binding to the nuclear membrane of the cells were confirmed by confocal microscopy

(70% of nuclei labelling, Fig. 6b and c). Efficient Mab414 transport in ARPE-19 cells (human retinal pigmentary epithelium) was validated by a 57% nuclear membrane staining in these cells (Fig. 6c). Additionally, a fluorescently labelled immunoglobulin (IgG-CF) was further transported across cell membranes (Fig. S9b, ESI†). Importantly, all controls in the absence of **MP1** resulted in endosomal entrapment and weaker punctate antibody fluorescence (left micrographs in Fig. 6b, c and Fig. S9b, S13, ESI†). Finally, proof of concept transport of antibodies in animal tissues was studied in murine cornea culture (Fig. 6d–g). The 3D confocal micrographs of the transfected corneas showed an excellent transport profile and nuclei labelling for the corneal epithelial cells by **MP1** (Fig. 6e). Again, control experiments in the absence of **MP1** showed weaker endosomal fluorescence signal (Fig. 6d). Fluorescein diacetate/propidium iodide live/dead staining was employed to check viability and integrity of the plasma membrane and the confocal micrographs confirmed an excellent viability of the cornea cells in the presence of **MP1**, which was nearly identical to the staining of untreated corneas

Cargo	Dextran 10 kDa	Saporin	Cre Recombinase	Dextran 40 kDa	IgG	Dextran 70 kDa
pI	—	9.40	9.60	—	6.6–7.2	—
MW / kDa	10	28.4	38.5	40	~ 150	70
R_H / nm	2.3	2.5	~ 4	4.5	5.4	6
Dim / nm	—	~ 6·4·3	~ 8·3·2	—	19·12·5	—

Fig. 6 Macromolecular cargos size and antibody transport in cells and tissues. (a) Table of the different cargos transported in this work (see ESI†). (b) HeLa cells were incubated with Mab414 and 0 (left) or 40 μM (right) **MP1**. (c) ARPE-19 cells incubated with Mab414 and 0 (left) or 50 μM (right) **MP1**. In (b and c), cells were incubated with the antibody for 1 h, followed by 2 h of incubation in serum supplemented media and fixation for immunofluorescence with an $Alexa_{594}$ labelled secondary antibody (red); nuclei were stained with DAPI (blue). (d) Cornea incubated with Mab414. (e) Cornea incubated with Mab414 and 150 μM **MP1**. In (d and e), left panel is a 3D reconstruction of the tissue; right panel is the maximal projection of the stack. (f) Cytotoxicity in corneas treated with 150 μM **MP1** by staining with propidium iodide (dead cells, red) and fluorescein diacetate (live cells, green). (g) Toxicity assay in cornea treated with Triton X-100. [Mab414] = 0.3 mg mL^{-1} in (b, d and e) and 0.15 mg mL^{-1} in (c). Scale bars are all 50 μm.
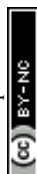
(Fig. 6f and Fig. S14a, ESI†). Triton X-100 showed the red stained micrographs, which confirmed the toxic profile of amphiphilic detergents (Fig. 6g and Fig. S14b, ESI†).

Conclusions

The objective of this work was to establish the potential of a rational strategy for the minimization of the number of cationic and hydrophobic residues in the development of membrane-targeted peptides capable of efficient but non-lytic transitory membrane disruption and macromolecular transport. The three key breakthroughs reported here are: (1) a rational strategy that allowed the discovery of oligoalanine peptide vehicles for protein transport with competitive efficiency compared to state of the art controls; (2) the non-toxic cytosolic delivery of exogenous monoclonal antibodies into animal tissues and (3) the assembly of supramolecular nanosized channels from a peptide sequence that is shorter than a lipid membrane. The discovery of penetrating peptide sequences showing different secondary structures such as random coils (*e.g.* CLIP6), alpha-helices (*e.g.* TP10, Pep-1) or beta-sheets (*e.g.* penetratin),[5,62–64] might have led to the conclusion that a particular secondary structure would not be required for membrane translocation. In addition, despite the evidence of conformational changes from natural (*e.g.* melittin),[65] synthetic (*e.g.* TP10, Pep-1),[6,63,66] and recent rational strategies,[67,68] the supramolecular control over the folding and assembly of small peptides with low cationic/amphiphilic character has not been sufficiently explored. The work described here introduces the selective non-lytic membrane perturbation from a peptide molecule shorter than a membrane leaflet. The peptide described here represents one of the simplest lineal peptide sequences with the minimum number of cationic and hydrophobic residues and yet capable of large protein (150 kDa) membrane transport, which allowed, to the best of our knowledge, the first example of antibody transport in animal tissues (cornea). It should be noted that since **MP1** is not covalently bound to its cargo, the supramolecular dynamic interactions between peptide, membrane and cargo could influence the optimal peptide concentration for a particular cargo and in a particular membrane. It should be noted that the behaviour of these peptides could be different in artificial and in cell membranes. For example, the enhancement of endocytosis, the different membrane composition and the dynamic character of the cargos employed (*i.e.* protein shape) can influence the size-selective transport observed for **MP1** in vesicles and cells. It should also be mentioned that in cell experiments, the transient membrane ruffling during endocytic or macropinocytic uptake of carrier and cargo might also lead to direct transport of the proteins.[69,70] Control experiments with reported peptide vehicles[10,12,38] confirmed **MP1** as a competitive candidate for protein delivery with an excellent biocompatibility and efficiency as well as a structural simplicity. Beyond these particular properties, the importance of this work relies on the application of a rational design strategy to minimize the number of cationic and hydrophobic residues for the "*en route*" modulation of peptide amphiphilicity for non-destructive transient membrane permeation and cargo transport. Even though there is still no FDA approved penetrating peptide vehicle,[71] this field is continuously improving in terms of carrier rational design and functional properties. The study presented here transversally covers the challenge of macromolecular transport from the molecular detail to the supramolecular level and up to the final functional applications in animal tissues. The simplicity of this new conceptual approach, together with the remarkable efficiency and broad scope of this methodology prompts new opportunities for the transport of macromolecules of biological interest and inspire the design and optimization of new synthetic membrane-targeted supramolecular transporters.

Conflicts of interest

There are no conflicts to declare.

Acknowledgements

References

1 G. Gasparini, E.-K. Bang, J. Montenegro and S. Matile, *Chem. Commun.*, 2015, **51**, 10389–10402.

2 G. Wiedman, S. Y. Kim, E. Zapata-Mercado, W. C. Wimley and K. Hristova, *J. Am. Chem. Soc.*, 2017, **139**, 937–945.

3 I. Lostalé-Seijo and J. Montenegro, *Nat. Rev. Chem.*, 2018, **2**, 258–277.

4 S. Y. Kim, A. E. Pittman, E. Zapata-Mercado, G. M. King, W. C. Wimley and K. Hristova, *J. Am. Chem. Soc.*, 2019, **141**, 6706–6718.

5 P. M. Fischer, *Med. Res. Rev.*, 2007, **27**, 755–795.

6 D. Kalafatovic and E. Giralt, *Molecules*, 2017, **22**, 1929.

7 M. Chiper, K. Niederreither and G. Zuber, *Adv. Healthcare Mater.*, 2017, **347**, 1701040.

8 M. J. Webber and R. Langer, *Chem. Soc. Rev.*, 2017, **46**, 6600–6620.

9 A. Méndez-Ardoy, I. Lostalé-Seijo and J. Montenegro, *Chem-BioChem*, 2018, **20**, 488–498.

10 M. C. Morris, J. Depollier, J. Mery, F. Heitz and G. Divita, *Nat. Biotechnol.*, 2001, **19**, 1173–1176.

11 S. Deshayes, M. Morris, F. Heitz and G. Divita, *Adv. Drug Delivery Rev.*, 2008, **60**, 537–547.

12 A. Erazo-Oliveras, K. Najjar, L. Dayani, T.-Y. Wang, G. A. Johnson and J.-P. Pellois, *Nat. Methods*, 2014, **11**, 861–867.

13 J. Yang, A. Bahreman, G. Daudey, J. Bussmann, R. C. L. Olsthoorn and A. Kros, *ACS Cent. Sci.*, 2016, **2**, 621–630.

14 F. Versluis, I. Tomatsu, S. Kehr, C. Fregonese, A. W. J. W. Tepper, M. C. A. Stuart, B. J. Ravoo, R. I. Koning and A. Kros, *J. Am. Chem. Soc.*, 2009, **131**, 13186–13187.

15 J. Allen, K. Najjar, A. Erazo-Oliveras, H. M. Kondow-McConaghy, D. J. Brock, K. Graham, E. C. Hager, A. L. J. Marschall, S. Dübel, R. L. Juliano and J.-P. Pellois, *ACS Chem. Biol.*, 2019, **14**, 2641–2651.

16 A. Steinauer, J. R. LaRochelle, S. L. Knox, R. F. Wissner, S. Berry and A. Schepartz, *Proc. Natl. Acad. Sci. U. S. A.*, 2019, **116**, 512–521.

17 J. R. LaRochelle, G. B. Cobb, A. Steinauer, E. Rhoades and A. Schepartz, *J. Am. Chem. Soc.*, 2015, **137**, 2536–2541.

18 S. E. Miller, Y. Yamada, N. Patel, E. Suárez, C. Andrews, S. Tau, B. T. Luke, R. E. Cachau and J. P. Schneider, *ACS Cent. Sci.*, 2019, **5**, 1750–1759.

19 I. Lostalé-Seijo, I. Louzao, M. Juanes and J. Montenegro, *Chem. Sci.*, 2017, **8**, 7923–7931.

20 K. Petkau-Milroy, M. H. Sonntag, A. H. A. M. van Onzen and L. Brunsveld, *J. Am. Chem. Soc.*, 2012, **134**, 8086–8089.

21 S. A. Bode, I. C. Kruis, H. P. J. H. M. Adams, W. C. Boelens, G. J. M. Pruijn, J. C. M. van Hest and D. W. P. M. Löwik, *ChemBioChem*, 2016, **18**, 185–188.

22 S. I. Lim, C. I. Lukianov and J. A. Champion, *J. Controlled Release*, 2017, **249**, 1–10.

23 B. M. de Ronde, N. D. Posey, R. Otter, L. M. Caffrey, L. M. Minter and G. N. Tew, *Biomacromolecules*, 2016, **17**, 1969–1977.

24 N. L. Benner, X. Zang, D. C. Buehler, V. A. Kickhoefer, M. E. Rome, L. H. Rome and P. A. Wender, *ACS Nano*, 2017, **11**, 872–881.

25 E. Derivery, E. Bartolami, S. Matile and M. Gonzalez-Gaitan, *J. Am. Chem. Soc.*, 2017, **139**, 10172–10175.

26 S. Ulrich, *Acc. Chem. Res.*, 2019, **52**, 510–519.

27 H. Fernández-Caro, I. Lostalé-Seijo, M. Martínez-Calvo, J. Mosquera, J. L. Mascareñas and J. Montenegro, *Chem. Sci.*, 2019, **10**, 7923–7931.

28 K. A. Mix, J. E. Lomax and R. T. Raines, *J. Am. Chem. Soc.*, 2017, **139**, 14396–14398.

29 J. A. Zuris, D. B. Thompson, Y. Shu, J. P. Guilinger, J. L. Bessen, J. H. Hu, M. L. Maeder, J. K. Joung, Z.-Y. Chen and D. R. Liu, *Nat. Biotechnol.*, 2015, **33**, 73–80.

30 H. H. Wang and A. Tsourkas, *Proc. Natl. Acad. Sci. U. S. A.*, 2019, **116**, 22132.

31 I. Canton, M. Massignani, N. Patikarnmonthon, L. Chierico, J. Robertson, S. A. Renshaw, N. J. Warren, J. P. Madsen, S. P. Armes, A. L. Lewis and G. Battaglia, *FASEB J.*, 2013, **27**, 98–108.

32 C. Liu, T. Wan, H. Wang, S. Zhang, Y. Ping and Y. Cheng, *Sci. Adv.*, 2019, **5**, eaaw8922.

33 E. A. Prasetyanto, A. Bertucci, D. Septiadi, R. Corradini, P. Castro-Hartmann and L. De Cola, *Angew. Chem., Int. Ed.*, 2016, **55**, 3323–3327.

34 R. Mout, M. Ray, Y.-W. Lee, F. Scaletti and V. M. Rotello, *Bioconjugate Chem.*, 2017, **28**, 880–884.

35 P. Yuan, H. Zhang, L. Qian, X. Mao, S. Du, C. Yu, B. Peng and S. Q. Yao, *Angew. Chem., Int. Ed.*, 2017, **56**, 12481–12485.

36 M. Marsh and A. Helenius, *Cell*, 2006, **124**, 729–740.

37 P. M. Matos, M. Marin, B. Ahn, W. Lam, N. C. Santos and G. B. Melikyan, *J. Biol. Chem.*, 2013, **288**, 12416–12425.

38 M. Akishiba, T. Takeuchi, Y. Kawaguchi, K. Sakamoto, H.-H. Yu, I. Nakase, T. Takatani-Nakase, F. Madani, A. Gräslund and S. Futaki, *Nat. Chem.*, 2017, **9**, 751–761.

39 N. J. Caron, S. P. Quenneville and J. P. Tremblay, *Biochem. Biophys. Res. Commun.*, 2004, **319**, 12–20.

40 A. Klimpel, T. Lützenburg and I. Neundorf, *Curr. Opin. Pharmacol.*, 2019, **47**, 8–13.

41 H. O. McCarthy, J. McCaffrey, C. M. McCrudden, A. Zholobenko, A. A. Ali, J. W. McBride, A. S. Massey, S. Pentlavalli, K.-H. Chen, G. Cole, S. P. Loughran, N. J. Dunne, R. F. Donnelly, V. L. Kett and T. Robson, *J. Controlled Release*, 2014, **189**, 141–149.

42 A. Lamiable, P. Thévenet, J. Rey, M. Vavrusa, P. Derreumaux and P. Tufféry, *Nucleic Acids Res.*, 2016, **44**, W449–W454.

43 S. Marqusee, V. H. Robbins and R. L. Baldwin, *Proc. Natl. Acad. Sci. U. S. A.*, 1989, **86**, 5286–5290.

44 A. Chakrabartty, T. Kortemme and R. L. Baldwin, *Protein Sci.*, 1994, **3**, 843–852.

45 A. Ho, S. R. Schwarze, S. J. Mermelstein, G. Waksman and S. F. Dowdy, *Cancer Res.*, 2001, **61**, 474–477.

46 M. Pazo, M. Juanes, I. Lostalé-Seijo and J. Montenegro, *Chem. Commun.*, 2018, **54**, 6919–6922.

47 N. Sakai and S. Matile, *J. Am. Chem. Soc.*, 2003, **125**, 14348–14356.

48 S. M. Kelly, T. J. Jess and N. C. Price, *Biochim. Biophys. Acta, Proteins Proteomics*, 2005, **1751**, 119–139.

49 W. Li, F. Nicol and F. C. Szoka, *Adv. Drug Delivery Rev.*, 2004, **56**, 967–985.

50 F. Hullin-Matsuda, T. Taguchi, P. Greimel and T. Kobayashi, *Semin. Cell Dev. Biol.*, 2014, **31**, 48–56.

51 L. M. Reid, C. S. Verma and J. W. Essex, *Drug Discovery Today*, 2019, **24**, 1821–1835.

52 S. J. Marrink, H. J. Risselada, S. Yefimov, D. P. Tieleman and A. H. de Vries, *J. Phys. Chem. B*, 2007, **111**, 7812–7824.

53 L. A. Patel and J. T. Kindt, *Soft Matter*, 2016, **12**, 1765–1777.

54 S. Matile and N. Sakai, *The Characterization of Synthetic Ion Channels and Pores*, Wiley-Blackwell, Weinheim, Germany, 2006.

55 H. D. Herce, A. E. Garcia, J. Litt, R. S. Kane, P. Martin, N. Enrique, A. Rebolledo and V. Milesi, *Biophys. J.*, 2009, **97**, 1917–1925.

56 T. M. Fyles, *Acc. Chem. Res.*, 2013, **46**, 2847–2855.

57 L. Li, T. Wan, M. Wan, B. Liu, R. Cheng and R. Zhang, *Cell Biol. Int.*, 2015, **39**, 531–539.

© 2021 The Author(s). Published by the Royal Society of Chemistry

RSC Chem. Biol., 2021, **2**, 503–512 | 511

58 P. Aimar, M. Meireles and V. Sanchez, *J. Membr. Sci.*, 1990, **54**, 321–338.

59 G. Meinke, A. Bohm, J. Hauber, M. T. Pisabarro and F. Buchholz, *Chem. Rev.*, 2016, **116**, 12785–12820.

60 A. N. Zelikin, C. Ehrhardt and A. M. Healy, *Nat. Chem.*, 2016, **8**, 997–1007.

61 T. A. Slastnikova, A. V. Ulasov, A. A. Rosenkranz and A. S. Sobolev, *Front. Pharmacol.*, 2018, **9**, 1208.

62 S. H. Medina, S. E. Miller, A. I. Keim, A. P. Gorka, M. J. Schnermann and J. P. Schneider, *Angew. Chem., Int. Ed.*, 2016, **55**, 3369–3372.

63 M. Magzoub, L. E. G. Eriksson and A. Gräslund, *Biochim. Biophys. Acta*, 2002, **1563**, 53–63.

64 U. Langel, *Cell-penetrating peptides: methods and protocols*, Humana Press, Totowa, NJ, USA, 2011.

65 C. E. Dempsey and G. S. Butler, *Biochemistry*, 1992, **31**, 11973–11977.

66 R. Rennert, I. Neundorf and A. G. Beck-Sickinger, *Adv. Drug Delivery Rev.*, 2008, **60**, 485–498.

67 S. Hyun, Y. Choi, H. N. Lee, C. Lee, D. Oh, D.-K. Lee, C. Lee, Y. Lee and J. Yu, *Chem. Sci.*, 2018, **9**, 3820–3827.

68 W. He, X. Xing, X. Wang, D. Wu, W. Wu, J. Guo and S. Mitragotri, *Adv. Funct. Mater.*, 2020, 1910566.

69 M. Akishiba and S. Futaki, *Mol. Pharmaceutics*, 2019, **16**, 2540–2548.

70 H. Hirose, T. Takeuchi, H. Osakada, S. Pujals, S. Katayama, I. Nakase, S. Kobayashi, T. Haraguchi and S. Futaki, *Mol. Ther.*, 2009, **20**, 984–993.

71 J. Xie, Y. Bi, H. Zhang, S. Dong, L. Teng, R. J. Lee and Z. Yang, *Front. Pharmacol.*, 2020, **11**, 697.